Field of first magnetic flux entry and pinning strength of superconductors for rf application measured with muon spin rotation

T. Junginger,[1,2,*] S. H. Abidi,[3] R. D. Maffett,[4] T. Buck,[5] M. H. Dehn,[5] S. Gheidi,[3] R. Kiefl,[5,6] P. Kolb,[7] D. Storey,[8,6] E. Thoeng,[5,6] W. Wasserman,[5] and R. E. Laxdal[6]

[1]*Engineering Department, Lancaster University, Lancaster LA1 4YW, United Kingdom*
[2]*Cockcroft Institute, Warrington WA4 4AD, United Kingdom*
[3]*University of Toronto, Toronto, ON M5S, Canada*
[4]*University of Waterloo, Waterloo, ON N2L 3G1, Canada*
[5]*University of British Columbia, Vancouver, BC V6T 1Z4, Canada*
[6]*TRIUMF Canada's National Laboratory for Particle and Nuclear Physics, Vancouver, BC V6T 2A3, Canada*
[7]*Brookhaven National Laboratory, Upton, New York 11973-5000, USA*
[8]*University of Victoria, Victoria, BC V8P 5C2, Canada*

(Received 6 December 2017; published 16 March 2018)

The performance of superconducting radiofrequency (SRF) cavities used for particle accelerators depends on two characteristic material parameters: field of first flux entry H_{entry} and pinning strength. The former sets the limit for the maximum achievable accelerating gradient, while the latter determines how efficiently flux can be expelled related to the maximum achievable quality factor. In this paper, a method based on muon spin rotation (μSR) is developed to probe these parameters on samples. It combines measurements from two different spectrometers, one being specifically built for these studies and samples of different geometries. It is found that annealing at 1400 °C virtually eliminates all pinning. Such an annealed substrate is ideally suited to measure H_{entry} of layered superconductors, which might enable accelerating gradients beyond bulk niobium technology.

DOI: 10.1103/PhysRevAccelBeams.21.032002

I. INTRODUCTION

Superconducting radiofrequency (SRF) cavities have been used to increase the energy of charged particles for more than 50 years [1]. The material of choice is niobium, the element with the highest critical temperature and critical fields. The performance of these cavities is usually expressed in a plot of the quality factor as a function of the accelerating gradient, see Fig. 1. The maximum achievable value for both quantities is related to the intrinsic material properties but also to the surface preparation. Depending on application, different recipes consisting of baking—under vacuum or in a gas atmosphere—and chemical treatments are applied.

The maximum accelerating gradient can be limited by several mechanisms including field emission, quench, and a strong decrease of the quality factor with accelerating gradient at high fields (Q-drop); in general the critical field of the material is not reached. The most common "recipe" for preparing cavities is the so-called "ILC" or "high gradient recipe" where the cavities receive a deep etch of 120 μm by either electropolishing (EP) or buffered chemical polishing (BCP), followed by baking at 800 °C for 4 hours to degas hydrogen and a final flash EP of 5–10 μm. A final low temperature bake-out at 120 °C for 24–48 hours in vacuum is applied to increase the peak field performance [2]. Cavities prepared by this high gradient recipe are usually limited by field emission or quench. These limiting mechanisms are specific to rf fields and related to the cleanliness of the surface and contaminants. They are not fundamental limitations of the material itself. It would be beneficial to characterize materials in terms

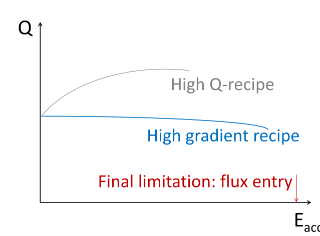

FIG. 1. Generic plot of the quality factor Q as a function of the accelerating gradient.

*Tobias.Junginger@lancaster.ac.uk

of H_{entry} as a function of surface and bulk treatments using DC methods without having to build an entire cavity. One potential method would be magnetometry. However, interpretations of results obtained by this technique are often ambiguous due to geometrical effects and pinning. Muon spin rotation and relaxation (μSR) is an alternative method that can be used to directly monitor the magnetic field inside the sample. It is a local probe which in principle can detect the field at specific locations in the sample. As such it provides information which is complementary to bulk methods such as magnetometry.

Recently, to reach high quality factors, a treatment procedure has been established baking cavities at 800 °C and injecting nitrogen gas at the end of this treatment. Consequently, cavities receive a light chemical etch to remove the outermost layer [3]. This "high Q-recipe" limits the accelerating gradients to lower values than the high-gradient recipe but enables quality factors close to the theoretical limit set by losses from thermally activated quasiparticles. These are fundamental to superconductors operated under rf fields above 0 K. To achieve highest quality factors especially with such cavities it is necessary to avoid trapping of external magnetic flux. Generally magnetic shielding is applied to reduce the Earth's magnetic field to a small fraction, but for ultimate performance, expulsion of the residual flux is necessary. Flux expulsion depends on the cooling dynamics around the critical temperature of the material T_{c} [4,5] and its pinning strength [6]. The μSR technique allows measurement of the magnetic flux inside a sample. By choosing an appropriate sample and field configuration, it enables measurement of the pinning strength of test samples.

The first application of μSR to SRF materials has been reported in 2013. Using the TRIUMF surface muon beam, Grassellino et al. [7] characterized samples cut out from cavities using the LAMPF spectrometer. These studies used a geometry that allowed comparison of the pinning strength of the different samples. In this paper we present complementary studies that aim to reveal the field of first flux entry H_{entry}. For this purpose samples of ellipsoidal geometry have been produced. In the experiments reported in [7], the magnetic field was applied perpendicular to the sample surface, unlike in accelerating cavities. To resemble the field geometry of SRF cavities, a spectrometer that allows the application of fields of up to 300 mT parallel to the sample surface was built. The combination of the different sample shapes and field geometries now allows the determination of the field of first flux entry and the pinning strength of the same samples as a function of surface and bulk treatments.

II. EXPERIMENTAL SETUP AND TECHNIQUE

Muon spin rotation [8,9] is a powerful condensed matter technique with many applications in magnetism and superconductivity. For example it can be used to understand superconductors in terms of their magnetic-phase diagram and penetration depth, as well as to characterize impurities based on muon diffusion. In the early 1970s, new high-intensity, intermediate-energy accelerators were built at PSI (Paul Scherrer Institute), TRIUMF (TRI-University Meson Facility), and LAMPF (Los Alamos Meson Physics Facility). These new "meson factories" produced pions (and therefore muons) at a rate several orders of magnitude more than previous sources—and in doing so, ushered in a new era in the techniques and applications of μSR.

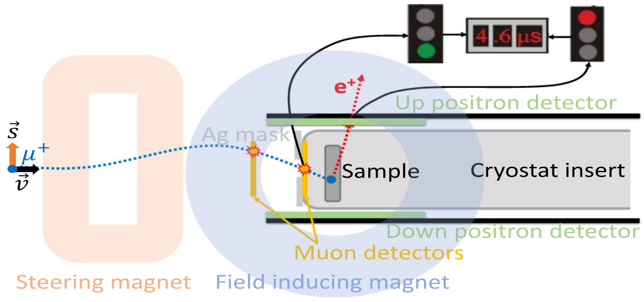

(a)

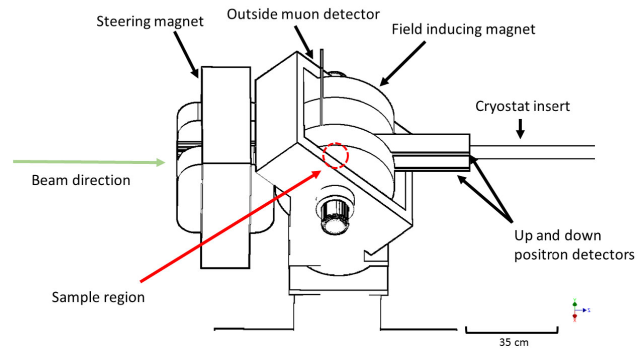

(b)

FIG. 2. (a) Schematic displaying the components of the HPF spectrometer and the beam trajectory (b) 3D render of the spectrometer. In the LAMPF spectrometer (not shown) the orientation of the magnetic field is parallel to muon momentum, therefore a steering magnet is not required.

A. Measurements in strong parallel fields

In order to allow for measurements in parallel magnetic fields of up to 300 mT, resembling the field geometry of SRF cavities, a dedicated spectrometer named High Parallel Field apparatus (HPF) has been added to the TRIUMF μSR M20 facility [10]. Due to the presence of the Lorentz force experienced by the muons in parallel geometry, the field that is used to probe the sample also bends the muon trajectory. Therefore, an upstream steering magnet is used to pre-steer off-axis and the applied field at the sample bends the particles back to the sample, see Fig. 2(a).

B. Obtaining the asymmetry function

For the experiments presented here, surface muons are emitted from a production target 100% spin polarized

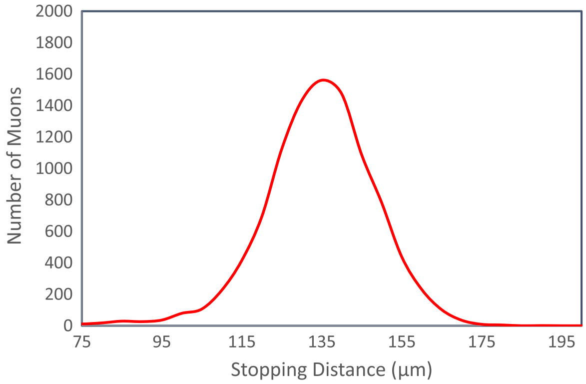

FIG. 3. Muon stopping distance in Nb as simulated by TRIM. The simulation takes into account all obstacles the muons encounter in their path such as beamline windows and scintillators.

with momentum and energy of 29.8 MeV/c and 4.1 MeV $+/-6\%$ respectively. They are implanted one at a time into the sample. These muons have an average stopping distance of 130 μm in niobium, as simulated by TRIM [11], see Fig. 3. When the muon decays (mean life time $= 2.197$ μs), it emits a fast positron preferentially along the direction of its spin at the time of the decay. By detecting the rate of emitted positrons as a function of time with two detectors placed symmetrically around the sample, here "up" and "down," the time evolution of the spin precession of the muon and therefore the magnetic field properties experienced by the muon can be inferred from the time dependent asymmetry in the positron decay

$$Asy(t) = \frac{N_U(t) - \alpha N_D(t)}{N_U(t) + \alpha N_D(t)} = A \cdot P(t). \qquad (1)$$

Here, $N_U(t)$ is the number of counts in the up detector and $N_D(t)$ is the number of counts in the down detector. The parameter α is added to account for detector efficiencies and to remove any bias caused by uneven solid angles. In the case where the detector efficiencies are identical, α assumes a value of 1, A is the initial asymmetry, while the depolarization function $P(t)$ signifies the change of asymmetry with time.

The aim of this experiment is to measure the fraction of the surface area probed by the muon beam which is in a field free Meissner state. Samples are placed in a cryostat surrounded by field inducing coils. For field penetration measurements, samples are cooled to below T_c (2.5 K is common) in zero field and then a static magnetic field is applied perpendicular to the initial spin polarization to probe if field has penetrated the sample. Specifically, the polarization signal gives information on the volume fraction of the host material sampled by the muon that does not contain magnetic field. This signal can be used to characterize the superconducting state, particularly the transition from Meissner to vortex state.

The muon intensity and count rate are such that the decay positrons can be counted one by one. Before implantation in the sample, the muons first pass through an initial muon counter (scintillator) starting an electronic clock, see Fig. 2. A silver mask with an 8 mm diameter hole in the center is used to restrict the muons to the center of the sample. A second muon counter behind the silver mask probes whether the muon went through the hole or was stopped by the mask. Only if the muon has been detected by both scintillators is its emitted decay positron counted. The spin-polarized muons are implanted into the sample, and quickly stop at interstitial sites in the bulk. The clock is stopped for each muon by its decay positron. Usually about 0.5 million muons are used to obtain one spectrum.

C. Polarization functions

If no magnetic field has entered the sample the depolarization of the muons is caused by the internal dipolar fields. Since these fields are randomly distributed, each muon will sense a different field orientation resulting in a quick loss of polarization. In the case of a static random field distribution, e.g., nuclear dipole fields, and the absence of muon diffusion, the muon spin polarization is given by the static zero field Gaussian Kubo-Toyabe function [12]

$$P_{ZF}^{stat}(t) = \frac{1}{3} + \frac{2}{3}[1 - (\sigma t)^2] \exp\left[-\frac{1}{2}(\sigma t)^2\right], \qquad (2)$$

where σ is the width of the dipolar field distribution. The function is characterized by an initial Gaussian shape and assumes 1/3 for long times. The initial part is explained by the Gaussian distributed nuclear magnetic dipolar fields from neighboring Nb nuclear spins that influence the muon spins. The relaxation to 1/3 of the initial value is due to the component of local fields along initial direction of polarization, i.e. 1/3 of the muons are polarized along the axis of initial polarization [12]. Equation (2) is only applicable to muons being static after initial trapping in static fields. Internal field dynamics, resulting either from the muon hopping from site to site or from fluctuations of the internal fields themselves, can be accounted for by using the strong collision approximation. This model assumes that the local field changes its direction at a time t according to a probability distribution

$$p(t) = \exp(-\nu t), \qquad (3)$$

with the hop rate ν. In the strong collision model, the field after each "collision" assumes a random value from the internal distribution, entirely uncorrelated with the field before the collision. The resulting expression is the dynamic Kubo-Toyabe (dynKT) depolarization function [12]

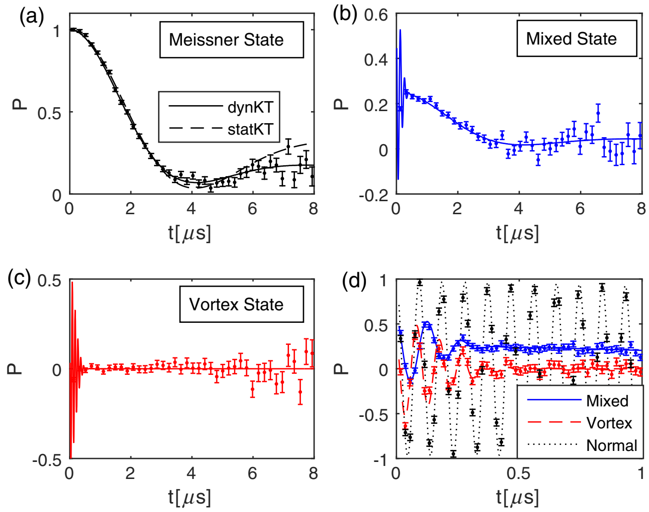

FIG. 4. Polarization function in different states. (a) In the Meissner state the depolarization is caused by randomly orientated nuclear dipole fields resulting in the characteristic dynamic Kubo-Toyabe polarization function. For comparison a fit to the static Kubo-Toyabe polarization function is plotted as well. This fit does not give a good representation for longer times. (b) In the mixed state, which is defined by coexisting macroscopic areas in the Meissner and vortex state, the Kubo-Toyabe polarization function is combined with a fast decaying oscillating function. (c) In the vortex state all muons sense the external field and there is no signature of the Kubo-Toyabe polarization function left. Here the strong damping is caused by the non uniformity of the vortex field structure. (d) In the normal state all muons probe the same field yielding weaker damping. Note the different time scale in this subplot.

$$P_{\mathrm{ZF}}^{\mathrm{dyn}}(t) = P_{\mathrm{ZF}}^{\mathrm{stat}}(t)\exp(-\nu t) + \nu\int_0^t dt'\{P(t-t')P_{\mathrm{ZF}}^{\mathrm{stat}}(t')\exp(-\nu t')\}, \qquad (4)$$

For large values of $\nu P(T)$ will assume an exponential decay shape and the recovery to $1/3$ is completely suppressed. An overview of depolarization functions commonly used in muon spin rotation experiments can be found in [8].

In the case of RRR niobium (RRR > 300), the muon is substantially diffusing in the material and the dynamic Gaussian-Kubo-Toyabe function Eq. (4) is applicable, see Fig. 4(a). As the applied field is increased, flux begins to penetrate the sample. As a result of its influence on the precession frequency of the muons, the amplitude of the Gaussian portion of the Kubo-Toyabe function decreases. The total polarization function will become a sum of two terms. The first one is the dynamic Kubo-Toyabe function with a reduced amplitude. The second term is a damped oscillating function yielding the complete polarization function as displayed in Fig. 4(b):

$$P(t) = f_0 \cdot P_{\mathrm{ZF}}^{\mathrm{dyn}}(t) + f_1 \cdot \exp\left(-\frac{1}{2}\Delta^2 t^2\right)\cdot\cos\left(\omega t + \frac{\pi\phi}{180}\right) \qquad (5)$$

with

$$\omega = \gamma_\mu H_{\mathrm{int}}, \qquad (6)$$

where $\gamma_\mu = 2\pi \cdot 13.55$ KHz/G is the gyromagnetic ratio of the muon and ϕ a phase which can depend on the external field. The internal field H_{int} has to be interpreted as the most probable internal field seen by the muons. In the normal state $H_{\mathrm{int}} = H_{\mathrm{a}}$, where H_{a} is the applied field, holds. For the mixed and the vortex state this is not the case. Here, H_{int} depends on the structure of the vortex shape. For a detailed description how the polarization function depends on the vortex shape refer to Ref. [13]. The value of f_0 compared to its initial low field value is a measure of the volume fraction being in the field free Meissner state. When completely in the Meissner state, there is no field in the sample and f_0 is maximized. Upon transitioning to the mixed state, which is defined by coexisting macroscopic areas in the Meissner and vortex state, $P(t)$ assumes the form of a heavily damped oscillation [Fig. 4(c)].[1] Now the muons precess with varying frequencies that depend on their distance from the intruding vortices. As the field strength increases further, f_0 will assume 0 when the whole area probed by the muons is in the vortex state. The damping of the oscillation will eventually become much weaker signifying that sample is in the normal state. In this state, the polarization implies that the muons are precessing largely with the same frequency since magnetic flux affects all sites almost uniformly. It is the existence of nuclear dipolar fields which adds slight damping to the signal.

D. Normal state calibration

We define the field of first flux entry when f_0 assumes a value significantly lower compared to its value at zero field. In the case of a pin free sample with no geometric edge boundary, that will happen suddenly in a sharp transition. Geometry and impurities can delay the flux penetration as mentioned above. Additionally, f_0 will also decrease as a function of field in the Meissner state since the muon will also precess in the external field outside of the sample before implantation. This can be accounted for by measuring the phase ϕ above the critical temperature T_{c} as a function of the applied field H_{a}. The relation $\phi(H_{\mathrm{a}})$ is subsequently used to correct the measured value of f_0, $f_{0|\,\mathrm{measured}}$, to physical meaningful values

$$f_0(H_{\mathrm{a}}) = \frac{f_{0|\,\mathrm{measured}}}{\cos\phi(H_{\mathrm{a}})}. \qquad (7)$$

Since the rotation of the muon spin is proportional to the magnetic field strength, a linear relation between $\phi(H_{\mathrm{a}})$ is expected and could be experimentally verified for both spectrometers, see Fig. 5. The effect is stronger for the

[1]Note that the damping is so strong that $P(t) = -1$ and $P(t) = 1$ are not observed.

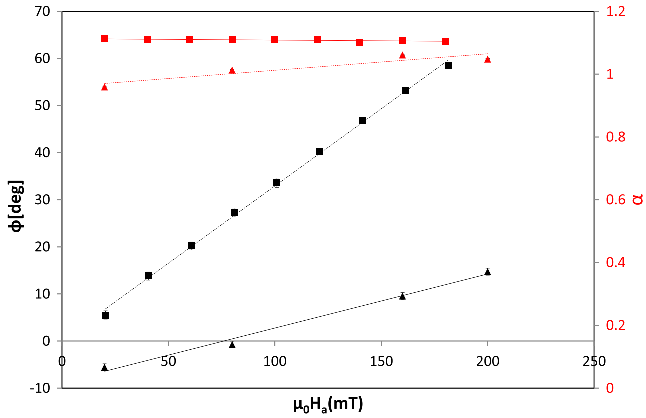

FIG. 5. Phase ϕ and α as a function of applied field H_a above T_c. Triangles/Squares are for the HPF/LAMPF spectrometer.

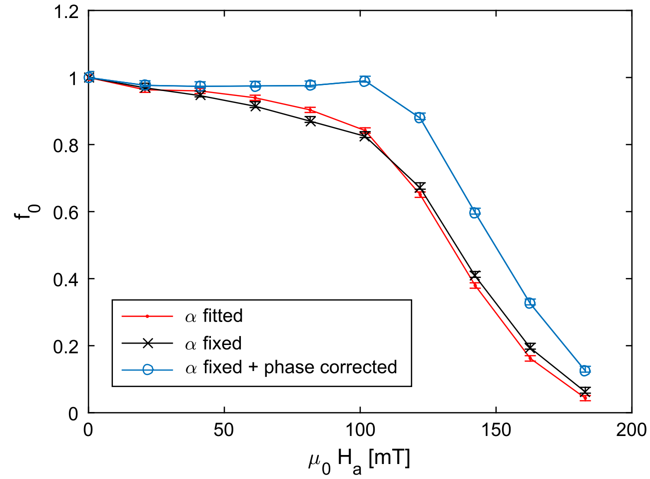

FIG. 6. Fit parameter f_0 as a function of applied field for a coin sample in transverse geometry (LAMPF). Fixing α from the normal state calibration yields a smother curve, while the phase correction eliminates the effect of reduced initial polarization due to spin rotation outside of the sample.

LAMPF than for the HPF spectrometer. HPF uses a magnet with an iron yoke confining the stray fields and therefore minimizes the time the muons spend in the external field before implantation in the sample. This yields less spin precession external to the sample compared to LAMPF which uses an air coil.

When the sample is in the Meissner state it is difficult to fit the parameters α and f_0 simultaneously. The strong damping implies that the polarization function never relaxes close to its initial value and f_0 and α become strongly correlated. If the sample is in the normal state, f_0 equals zero and the polarization function oscillates around zero, see Fig. 4(d). Therefore α can be precisely measured in the normal state above T_c and then be fixed for data obtained below T_c instead of being used as an additional fit parameter.

Intuitively, α should not depend on the external field, since it accounts for the detector efficiencies and alignment which should not be affected by the external field. However, experimentally it was found that α changes linearly with field for both spectrometers, see Fig. 5. In the HPF spectrometer the external magnetic field not only acts on the muon spin but also steers the beam before it enters the sample, which can result in a shift of the beam spot and therefore a field dependent α. For the LAMPF spectrometer, the field is applied in the direction of muon propagation. However, stray fields, misalignment, and imperfectly polarized beams can still yield a field dependent α. As for HPF, a linear, but weaker $\alpha(H)$ dependence was found, see Fig. 5. The linear $\alpha(H)$ relation allows for taking only a few measurements above T_c and using a linear correction function for calibration.

In the experiment, the magnetic field is controlled by setting the current I to the magnets. The most accurate way to derive the $B(I)$-relation is using the measurement in the normal state.

In summary, the normal state calibration serves three purposes: (1) Establish the $B(I)$ relation, (2) Correct for muon precession in the field outside of the sample, (3) Correct for drifts of the beam spot due to steering.

Experimentally it was found that a normal state calibration needs to be performed for every sample. While $\phi(B)$ and $B(I)$ only slightly change for each setup, the critical relation is $\alpha(B)$. Fig. 6 shows an example of a sample measured on LAMPF. Fixing α yields a smoother curve, especially visible here in the low field area. The phase correction shifts the whole curve up and enables a better estimation of $H_{a|\,\mathrm{entry}}$, effectively eliminating the effect of muon spin rotation outside of the sample.

E. Samples

Several sample types and fields geometries are used. Unless otherwise stated, all samples are made of RRR niobium, which specifies niobium with a RRR > 300. Coin samples of 3 mm thickness and 20 mm diameter are cut by water jet from flat sheets. Similar coins were cut by wire electrical discharge machining (EDM) from a 1.3 GHz cavity half-cell of TESLA shape at a location 45° from the equator as rotated toward the iris. This half-cell was made by deep drawing from a sheet of 3 mm thickness. These cylindrical samples can be tested in parallel and perpendicular field geometry. Figure 7(a) displays the initial perpendicular field configuration, while Fig. 7(b) shows the direction of applied magnetic field and muon propagation for the HPF spectrometer developed to test samples in a parallel field geometry.

Another set of samples were machined in the shape of a prolate ellipsoid. The dimensions are semimajor axis of 22.9 mm and semi-minor circular cross-section of 9.0 mm radius. Moreover, along the major axis, at one end there is a 21 mm deep 1/4–20 threaded hole which was used to hold

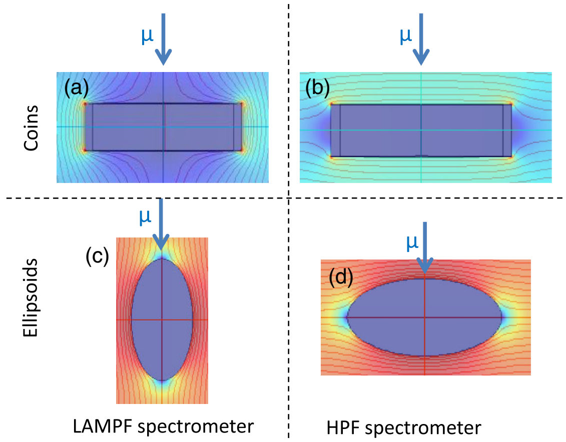

FIG. 7. Four generic arrangements of sample, muon and field direction using the LAMPF and HPF spectrometers. Red/blue color indicates areas of high/low magnetic field (compare to flux line density). The direction of the muon spin is always perpendicular to the beam direction, the sample surface and the applied field. (a) Note the high flux line density at the edges of the coin in the transverse geometry (LAMPF). (b) In the parallel geometry (HPF) the field enhancement at the edges is much weaker. (c,d) For the ellipsoid there is no edge boundary. Here the field will first nucleate at the equator, where the muons are implanted in the HPF setup. Simulations have been performed with Comsol Multiphysics assuming the samples to be in a perfect Meissner state (relative magnetic permeability $\mu_r = 0$).

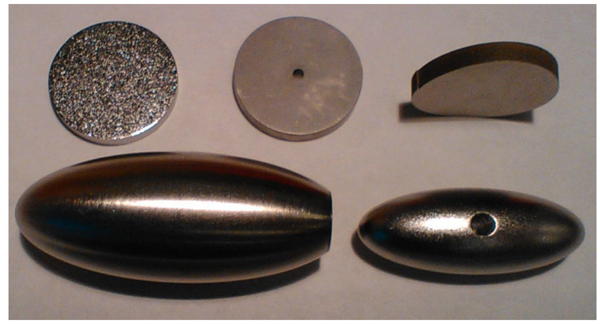

FIG. 8. Example of samples used in the experiment. Top, from left to right: Coins after BCP, after deposition of Nb3Sn (the whole in the middle was used to hang the sample in the furnace) and cut from a 1.3 GHz cavity half cell. Bottom: Ellipsoids used in LAMPF (left) and HPF (right).

the sample. These samples can be tested in the initial LAMPF spectrometer. Here, the magnetic field is applied along the major axis of the sample and the muons are being implanted on the tip of the sample, see Fig. 7(c). A fourth set of samples consists of smaller ellipsoids which can be used in the HPF spectrometer, see Fig. 7(d). These ellipsoids have the same aspect ratio as the larger ones but have been scaled down to a semi major axis length of 16 mm to fit the cryostat. To hold the sample, a 4/40 threaded hole is placed on the minor axis.

The samples were subjected to a variety of different treatments typical for SRF cavity processing. These included heat treatments in vacuum such as 120 °C bake for 48 hours and 800 °C degassing for 4 hours. Vacuum heat treatments at 1200 °C and 1400 °C for 4 hours each were also employed. Surface treatments include etching using both buffered chemical polishing (BCP) and electropolishing (EP) with various removals. To study materials other than niobium some samples were coated. For example, Fig. 8 displays a coin which has received a Nb3Sn coating using a thermal diffusion technique at Cornell University.

III. EFFECT OF PINNING AND GEOMETRY

A. Coins in transverse geometry

Consider first the coin sample with field applied perpendicular to the face [Fig. 7(a)]. When in the Meissner state, surface currents will be set up to cancel the field in the bulk. The magnetic field will be enhanced at the edges of the coin by a factor related to a demagnetization factor N by $H_{\mathrm{edge}} = H_{\mathrm{a}}/(1 - N)$ where H_{a} is the applied field. In the literature, N is often more specifically referred to as the magnetometric demagnetization factor to distinguish it from the fluxmetric (also known as ballistic) demagnetization factor N_{s}. The latter is related to flux penetration into the midplane of the samples. For non-elliptical shapes N and N_{s} both depend not only on the sample geometry but also on the susceptibility of the material χ [14]. Numerical calculations of N and N_{s} necessarily require a constant χ. For superconductors, $\chi = -1$ is only valid in case of complete shielding. Therefore, this concept is applicable to calculate H_{edge} from N, but not H_{entry} from N_{s}. For the latter, Brandt has developed a model which calculates magnetization curves $M(H_{\mathrm{a}})$ for some geometries and derives H_{entry} from its maximum.

For Type II superconductors when the applied field is such that the enhanced field at the edges reaches H_{c1}, the field will break into the edge such that the local field is reduced due to the rounding of the flux line. As the field increases the flux lines will cut further across the corner and eventually join at the center of the sample edge. This corresponds to $H_{\mathrm{a|\,entry}} = H_{\mathrm{a}}/(1 - N_{\mathrm{s}})$ and is higher than $H_{\mathrm{c1}} \cdot (1 - N)$ due to the so called edge boundary [15]. The flux line now crosses the full sample width and is driven inwards due to interaction with the surface currents.

In a pin-free sample the flux will move to the center since this represents the lowest energy position (minimum line tension), see Fig. 9. As the flux increases and vortices multiply, the vortex currents will repel so that the flux lines will redistribute and fill from the center to the outside edge. In our case for the transverse coin geometry (cylinder in axial field), with diameter $a = 20$ mm and thickness $b = 3$ mm, the demagnetizing factor is $N = 0.77$ meaning that $H_{\mathrm{a|\,edge}} = 0.23 H_{\mathrm{c1}}$. Brandt [15] derives the field of first flux entry (to the midplane) from the maximum $M(H_{\mathrm{a}})$,

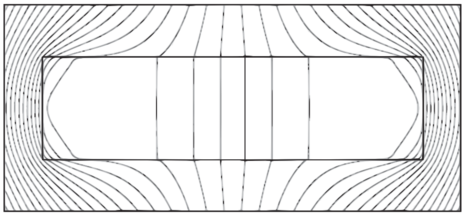

FIG. 9. Flux applied to a thin circular disk transverse to an applied field where $H_a > H_{a|\text{entry}}$. The field breaks in at the edges first at $H_{\text{edge}} < H_{a|\text{entry}}$. Above $H_{a|\text{entry}}$ the flux lines will move to the center of the sample, which is the position with lowest line tension. Redrawn after [15].

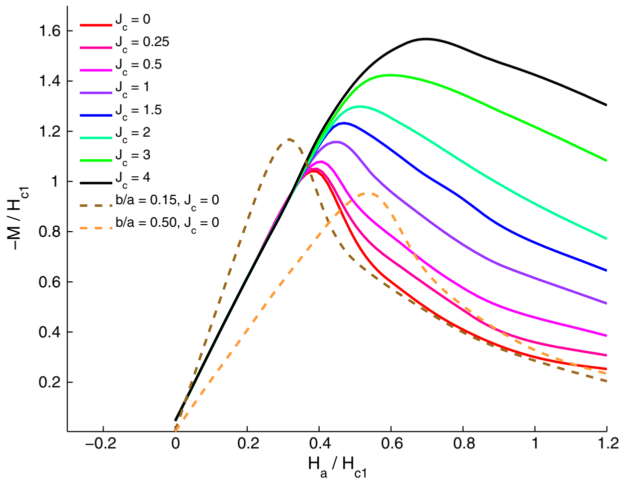

FIG. 10. Magnetization curves for a disk sample with different pinning and geometry. Solid lines correspond to the sample with b/a = 0.3 while the dash line correspond to pin-free sample with b/a = 0.15 and 0.50. The critical current density J_c is a measure of the pinning strength. The larger J_c the stronger the pinning. Adapted from [15].

where M is the magnetization. For a cylinder in an axial field he finds:

$$H_{a|\text{entry}} = \tanh\sqrt{0.67\frac{b}{a}} \cdot H_{c1} = 0.31 H_{c1}. \quad (8)$$

For a sample with pinning, the pinning centers act as additional barriers adding "resistance" to the mobility of vortices moving from the edges to the center and increasing $H_{a|\text{entry}}$ compared to the pin free case, see Fig. 10. Hence, introducing pinning into the material delays the entry of magnetic field into the center of the sample.

B. Parallel coin

In the parallel geometry [Fig. 7(b)], the sample coin is placed parallel to the applied field and the muons are applied to the coin face. The demagnetization factor in this radial geometry has been calculated by Chen *et al.* [16]. For our standard geometry (diameter $a = 20$ mm and thickness $b = 3$ mm), $N = 0.15$. To estimate $H_{a|\text{entry}}$ we cannot use a literature value of a fluxmetric demagnetization factor, since this concept relying on a constant χ is not applicable as mentioned above. Furthermore, for this radial geometry an approximation formula for $H_{a|\text{entry}}$ has not yet been derived to our knowledge. Brandt in [15] derives a formula for a long strip with rectangular cross section $a \times b$ with the field applied along a,

$$H_{a|\text{entry}} = \tanh\sqrt{0.36\frac{a}{b}} \cdot H_{c1}. \quad (9)$$

Since we are only interested in the inner area probed by the muons (8 mm diameter) this geometry should be applicable to our setup. This assumption will be reviewed later by comparing samples of different geometry and identical preparation. For our standard geometry (diameter $a = 20$ mm and thickness $b = 3$ mm) we find $H_{a|\text{entry}} = 0.91 H_{c1}$.

In this parallel geometry, the volume sampled by the muons is less sensitive to pinning. Flux could still be pinned at the corners before linking at the center (pinning enhanced edge boundary) but much less so than in the transverse geometry since no flux motion from the edges of the sample to its center is required as in the transverse geometry.

C. Ellipsoids

For the ellipsoidal geometry the edge boundary is eliminated. The inward directed driving force on the vortex ends by the surface screening currents is compensated by the vortex line length that increases for fluxoids that are closer to the ellipsoid axis—so pin-free ellipsoidal samples produce a uniform vortex flux density in the mixed state. The Meissner state is supported by screening currents that augment the field at the equator and reduce the field at the poles. When the flux at the equator reaches H_{entry}, which could be either the lower critical field H_{c1} or in case of a surface barrier the superheating field H_{sh}, fluxoids will nucleate at the equator and redistribute uniformly inside the superconductor due to vortex repulsion for a pin free sample.

In our geometry, the demagnetizing factor is $N = 0.13$ with $H_{a|\text{entry}} = 0.87 H_{\text{entry}}$ [15], where H_{entry} denotes the intrinsic field of first entry of the material. In the case of samples with pinning, the redistribution will be affected as the pinning centers will add a frictional component to the redistribution such that the fluxoids will tend to preferentially populate nearer the equator and will only gradually reach the poles as the applied field increases beyond $H_{a|\text{entry}}$.

The parallel field ellipsoid geometry with an application of muons at the equator [Fig. 7(d)] should be the least sensitive to pinning and is our preferred geometry to probe the intrinsic field of first flux entry H_{entry}.

D. Coated samples

Consider now a niobium sample coated with a thin layer of a material with larger T_c. If this layer is thinner than the

TABLE I. Geometrical normalizing factors for expected pin-free flux entry for the three sample types assuming $\mu_0 H_{c1}(0\text{ K}) = 174$ mT. For the shell geometry the edge boundary is eliminated yielding $H_{a|\text{entry}} = H_{\text{edge}} = (1-N)H_{c1}$.

Sample	SC type	N	$H_{a\|\text{entry}}/H_{c1}$	$\mu_0 H_0$ (2.5 K) [mT]
Transverse coin	bulk	0.77	0.31	50
Parallel Coin	bulk	0.15	0.91	146
Ellipsoid	bulk	0.13	0.87	140
Transverse coin	shell	0.77	0.23	37
Parallel Coin	shell	0.15	0.85	137
Ellipsoid	shell	0.13	0.87	140

implantation depth of the muons and measured above T_c of niobium but below T_c of the coating, the geometry will be a superconducting shell.

With the bulk of the sample being normal conducting and therefore not providing any pinning, the geometric boundary is eliminated since as soon as flux breaks into the corners the fluxoid will snap to the center for a pin free shell. For the case of the transverse coin $H_{a|\text{entry}} = H_{a|\text{edge}} = 0.23H_{c1}$, while for the superconducting shell in parallel geometry we expect $H_{a|\text{entry}} = 0.85H_{c1}$. For ellipsoidal shells the situation is similar to bulk ellipsoids in terms of magnetization except that after nucleation, the fluxoids will snap to the center since the flux line length in the superconducting shell is actually less near the ellipsoid axis so that pinning would be less dominant in resisting nucleated flux to move to the poles. Table I displays the demagnetization factor N and $H_{a|\text{entry}}/H_{c1}$ for all geometries. Note that in case of the ellipsoids, the field direction with respect to the sample geometry is identical in the two spectrometers and only the muon implantation site is changed. Therefore, N and $H_{a|\text{entry}}/H_{c1}$ are identical for the two ellipsoid arrangements.

E. Expected field of first entry

Measurements are typically performed at about 2.5 K. For the critical temperature of niobium 9.25 K [17] and assuming the empirical relation for the temperature dependance

$$H_{c1}(T) = H_{c1}(0)\left[1 - \left(\frac{T}{T_c}\right)^2\right] \tag{10}$$

$\mu_0 H_{c1}(2.5\text{ K}) \approx 161$ mT can be obtained, assuming $\mu_0 H_{c1}(0\text{ K}) = 174$ mT [17]. Finally, the expected field of first entry for a pin free niobium sample with no surface barrier

$$H_0(T) = \frac{H_{a|\text{entry}}}{H_{c1}} H_{c1}(T) \tag{11}$$

can be calculated. Table I displays $\mu_0 H_0(2.5\text{ K})$ for all geometries.

IV. RESULTS

A. Comparing geometries

We present several results from different samples first to illustrate the effect of the geometry. In these and subsequent plots the field is normalized to H/H_0 where H_0 corresponds to the expected entry field for a pin-free sample, with demagnetization and edge boundary considered, assuming $H_{c1}(0\text{ K}) = 174$ mT [17]. For the critical temperature of niobium 9.25 K and assuming the empirical relation for the temperature dependance Eq. (10), $H_{c1}(\text{T})$ is obtained individually for each curve. Table I gives the estimated H_0 values for the three geometries at the typical measurement temperature 2.5 K. Statistical fit errors are on the order of the size of the markers or smaller, see Fig. 6, and are for simplicity not displayed in subsequent plots. The resolution of the H_{entry} measurement is determined by the number of data points $f_0(H)$ taken in the area of transition from the Meissner to the vortex state. The uncertainty for the measured H is mostly affected by misalignment, which is estimated to be below 5° corresponding to less than 1 mT even at high field.

Figure 11(a) shows f_0 as a function of applied field for the four different sample/field arrangements used in this experiment. All these samples have received buffered chemical polishing (BCP), but no bakeout. The pinning strength is therefore expected to be rather strong. For all samples, f_0 stays above 0 beyond the expected field of first entry. The effect is most strongly pronounced for the coin in transverse geometry. In comparison, ellipsoid shaped samples in the same spectrometer (LAMPF) yield a geometry less sensitive to pinning. The HPF spectrometer is better suited for field of first entry measurements. Here, f_0 reaches a 0 value at a field closer to the predicted value for niobium of $H/H_0 = 1$. In Fig. 11(b) the samples are heat treated at 1400 °C. This virtually eliminates all pinning as the material is fully recrystallized at this temperature.

B. Transverse coin results

The results presented so far show that the transverse geometry is especially sensitive to pinning in the sample. In the following, this geometry will be used to test how various surface and bulk treatments can affect the pinning strength. For this study five samples were cut out from the same RRR niobium sheet. One sample received no further treatment while the others were chemically etched (BCP) to remove 100 μm material. Three of these samples were subsequently baked at 120 °C for 48 hours. Afterwards, two samples received additional surface treatments, one a 5 μm BCP and the other one a rinsing with hydrofluoric acid to remove and regrow the oxide layer. The results displayed in Fig. 12(a) show that the pinning strength is reduced by the initial BCP as the original damaged layer is removed. Further, it can be observed that low temperature baking and surface treatments after BCP show no effect.

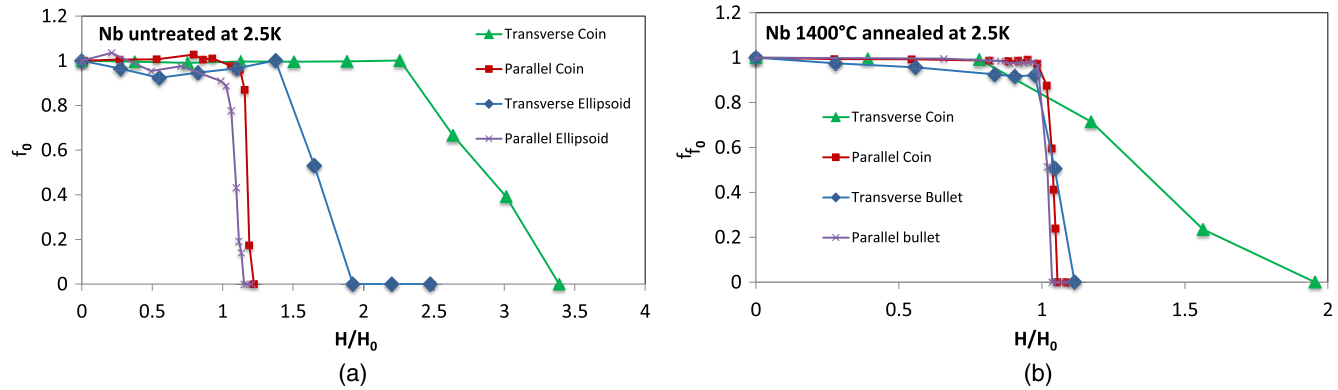

FIG. 11. Fit parameter f_0 signifying the volume fraction probed by the muons which is in the field free Meissner state as a function of applied field in four geometries. (a) Chemically etched samples with no heat treatment: The apparent differences in H/H_0 are correlated to the different sensitivity to pinning of the four geometries. (b) Annealing at 1400 °C virtually releases all pinning.

To get more information on how the flux breaks in for the case with pinning, a series of measurements were taken with different masking foils: a standard 8 mm aperture (4 mm radius), an annular mask blocking the center of the sample with an inner and outer radius of 4 and 6 mm, and a second annular mask with radii 6–8 mm. The results are plotted in Fig. 12(b), once again with fields normalized to the expected $H_{\mathrm{a|\,entry}}$ based on the geometry. The sample used for this test was first treated by a bulk buffered chemical polishing (BCP) removing 100 μm, followed by 120 °C baking in vacuum and a final 5 μm BCP. For this treatment the pinning is rather strong as can be seen from the curve obtained with the standard 0–4 mm mask, also displayed in Fig. 12(a). The flux is not driven to the center until the field reaches over two times the pin-free $H_{\mathrm{a|\,entry}}$, and is not fully saturated until over three times $H_{\mathrm{a|\,entry}}$.

Figure 12(c) shows results from a thinner coin cut from RRR Nb. This sample was first etched (BCP) and demonstrates the characteristics of strong pinning. The sample was then heat treated at 1400 °C, resulting in a significant decrease in pinning. When the annealed sample is etched again, removing 7 μm material, the pinning did not return.

In the next study the role of forming as a source of pinning is explored. Here the samples were cut using wire EDM from a 1.3 GHz half cell (dumb-bell). The formed samples are treated with standard BCP and 800 °C bake-out and are compared to flat samples with similar treatments. The results of the study are shown in Fig. 12(d). Pinning in formed samples delays flux entry to three times higher field as compared to the same sample after annealing at 1400 °C. A 800 °C treatment does relax pinning somewhat in both flat and formed cases.

C. Transverse ellipsoid results

The transverse ellipsoid is positioned as in Fig. 7(c) with the long axis coincident with the muon beam and aligned with the applied field. The muons are localized on the sample with a 8 mm diameter mask identical to the transverse sample study. Here the mask confines the muons to the pole of the ellipsoid. The ellipsoids received various bulk and surface treatments as with the coins. In general, pinning is less predominant in the ellipsoid due to the lower demagnetization factor. However, pinning is still a factor as the fluxoids will nucleate at the equator and must overcome pinning to move to the pole. Heat treatments to 1400 °C are shown to be effective to strongly reduce pinning as with the transverse coins. Figure 13(a) shows results from three ellipsoids with four hour heat treatments of 1400 °C, 1200 °C, and 800 °C respectively. In both 1400 °C and 1200 °C, the field entry has a sharp threshold characteristic of uniform entry while the 800 °C sample shows entry of fields at the pole for higher applied fields with an extended tail to $1.5H_0$.

Another set of studies was done comparing N-doped and non-N-doped material. The N-doping was done at FNAL [3]. The doping involves heating a sample to 800 °C for four hours and injecting N_2 gas near the end of the treatment. The sample was first tested directly after the doping procedure and again after removing 5 μm by electropolishing which yields high quality factors in SRF cavities [3]. The results from these samples are also displayed in Fig. 13(a).

D. Parallel ellipsoid results

The parallel ellipsoid geometry with the muons applied at the equator as displayed in Fig. 7(d) should be the least sensitive to pinning since the flux nucleates at the equator in the same location as the muons. The results of three samples tested in this geometry are displayed in Fig. 13(b). All samples were first etched (BCP) to remove 100 μm material. One sample was then annealed at 1400 °C. After the initial test it was baked at 120 °C for 48 hours together with one of the two samples which was not annealed.

E. Coated samples

This μSR method developed and commissioned using Nb samples has also been used to characterize Nb samples

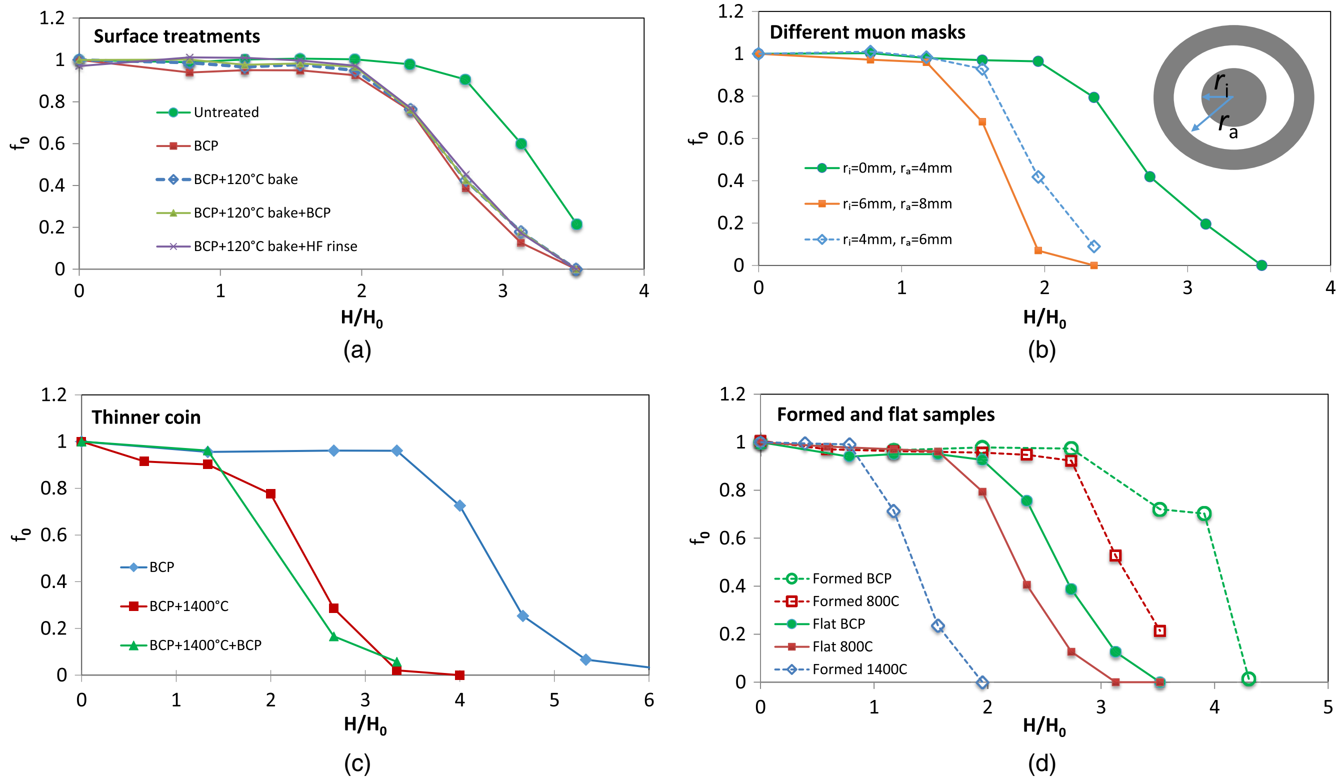

FIG. 12. Fit parameter f_0 signifying the volume fraction probed by the muons which is in the field free Meissner state as a function of applied field for coins in transverse geometry (LAMPF) at 2.5 K. (a) BCP removes the outer damaged layer and releases pinning. Additional surface treatments show no effect on the pinning strength. (b) Different masks, probing different areas on the sample visualize how flux breaks in from the corner of the sample in the transverse coin geometry. (c) A smaller coin of 0.8 mm thickness and 18 mm diameter. The sample was first etched (BCP), followed by annealing (1400 °C) and another BCP. The BCP treatment after annealing does not alter the pinning strength. (d) Formed and flat geometries. Formed samples are denoted with dashed lines. This plot shows that forming increases the pinning strength, which is virtually eliminated by a subsequent annealing at 1400 °C.

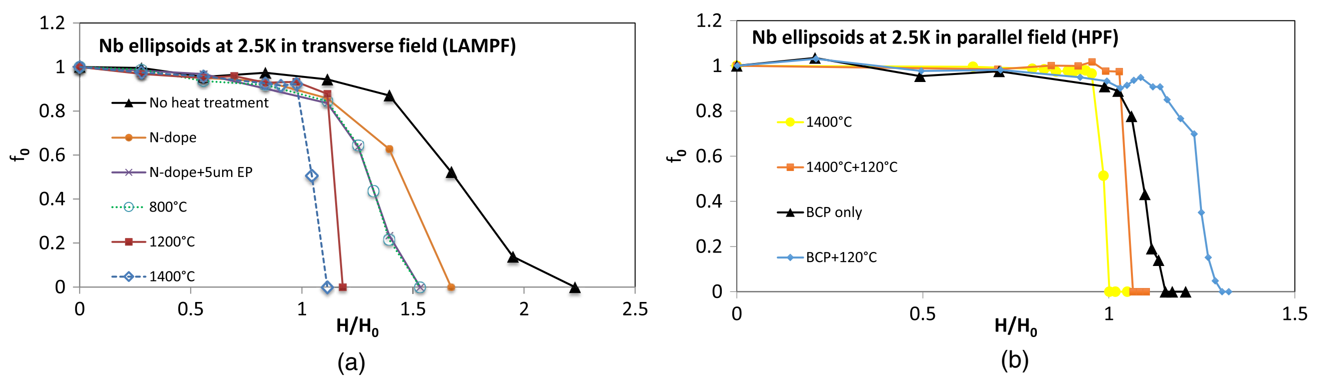

FIG. 13. Fit parameter f_0 signifying the volume fraction probed by the muons which is in the field free Meissner state as a function of applied field for ellipsoid samples with different heat treatments measured in (a) the LAMPF spectrometer and (b) the HPF spectrometer.

coated with higher T_c materials. For example, collaborators at Cornell University have coated a standard Nb coin and ellipsoids for both spectrometers with a 2 μm coating of Nb_3Sn using their standard recipe [18]. The same coin sample was tested in both transverse and parallel geometry. In total all four available arrangements (Fig. 7) have been used to test this coating, see Fig. 14(a).

The data is normalized to H_0 as expected for Nb for convenient comparison with data presented above. The transverse ellipsoid sample has also been measured at

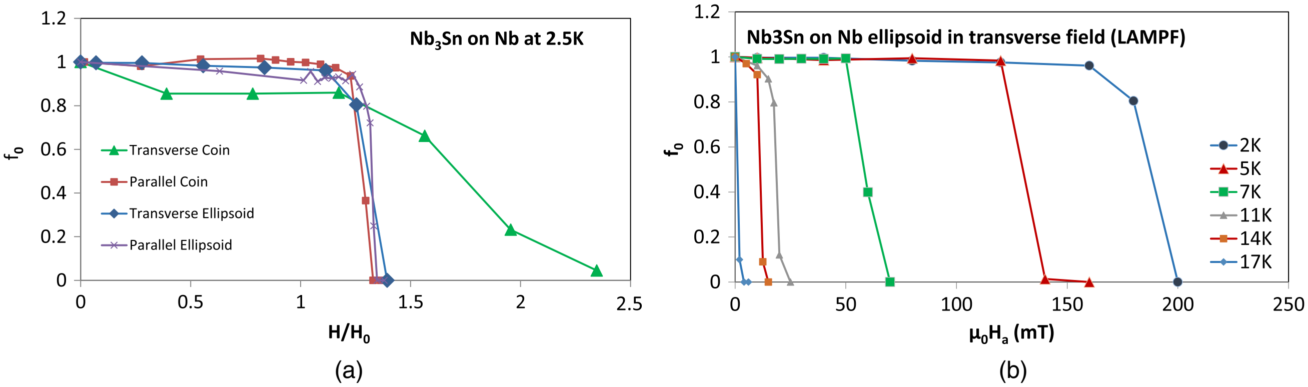

FIG. 14. Fit parameter f_0 signifying the volume fraction probed by the muons which is in the field free Meissner state as a function of applied field for 2 μm Nb_3Sn on Nb (a) in different geometries (b) of an ellipsoid in transverse field measured at different temperatures in the LAMPF spectrometer.

several temperatures above and below 9.25 K, the critical temperature of niobium, see Fig. 14(b).

V. DISCUSSION

The μSR technique applied to SRF materials has been extended by adding a dedicated spectrometer enabling measurements in strong parallel fields to the TRIUMF μSR facility and using different sample geometries. These various sample shapes and test configurations are crucial to the interpretation of the results in terms of pinning strength and field first flux penetration H_{entry}.

A. Sensitivity to pinning in different geometries

First, samples which have received only a chemical polishing but no heat treatment have been compared to samples which have been annealed at 1400 °C, see Fig. 11, representing the cases of strong and weak pinning, respectively. Flux reaches the area probed by the muons in different ways depending on the chosen geometry. In the transverse coin geometry (LAMPF) flux will first penetrate the edges of the disk. For samples with strong pinning (no heat treatment) the center of the sample, where the muons are implanted, is only fully penetrated at a field 3.5 times higher than the expected field of first flux entry. This geometry is therefore well suited to measure qualitatively the pinning strength for different surface treatments. Comparing results obtained with different annular masks, probing different areas on the sample surface, we find that the field breaks in near $H_{\mathrm{a|\,entry}}$ at large radii but does not migrate to the center as would be expected for a pin-free case, see Fig. 12(b). These results are a strong confirmation of the role of pinning as a source of flux drag that inhibits redistribution of the penetrating flux into the sample center.

The parallel ellipsoid geometry (HPF spectrometer) should be the least sensitive to pinning due to the low demagnetization factor and because the muons are implanted at the equator where the field will first nucleate. However, the results [Fig. 13(b)] suggest that some sensitivity to pinning still exists for this geometry since the field of first entry, as sampled by the muon, still shows dependence on the 1400 °C anneal treatment.

Note that the muons are not stopped directly at the surface but at about 130 μm deep in the bulk. For the spot probed by the muons to remain in a field free state above H_{nucleate}, flux needs to be pinned in this 130 μm layer. For comparison, the ellipsoid has a radius of 6.3 mm at the equator. The hypothesis that a layer of a few μm can pin vortices is consistent with the finding that a nitrogen doped transverse ellipsoid showed stronger pinning compared to one which was only baked at the same temperature of 800 °C, see Fig. 13(a). Furthermore, after an additional electropolishing of only 5 μm, the pinning strength of this sample was found to be identical to the one without doping.

Pinning is an important parameter for SRF applications. In order to achieve the lowest residual resistance, as required for CW applications, shielding of the earth's magnetic field alone is not sufficient, but residual flux needs also to be expelled [4,5]. In [6] flux expulsion for different cavity treatments has been addressed by investigating full cavities. However, there are only a few dedicated material studies using magnetometry to directly measure the pinning strength of SRF materials. Casalbuoni *et al.* have used cylinders cut from sheets [19]. The advantage of our method is that the muons are implanted locally allowing to distinguish better between geometrical edge pinning and intrinsic pinning from the material itself. Ashavai *et al.* avoid geometrical constraints by using long cylinders with very low demagnetization factors [20]. This method, unlike ours, does therefore not allow the use of samples cut out from niobium sheet or from cavities characterized by rf and temperature mapping.

B. Effect of heat and surface treatments on the pinning strength

Bulk pinning in the material changes considerably depending on heat treatments. A 1400 °C annealing virtually eliminates pinning and subsequent BCP does not erase this effect. For such annealed RRR niobium samples, measured in the HPF spectrometer with the field applied parallel to the sample surface, the field of first flux entry H_{entry} is found consistent with literature values of H_{c1}, see Fig. 11(a). Generally, surface treatments such as 120 °C, HF rinsing, and BCP of a few μm do not change the bulk pinning strength, indicating that beyond the gross removal of surface pollution, the pinning is more dependent on the bulk properties, see Fig. 12. Nitrogen doping however yields a slight increase in pinning strength which is erased by a subsequent 5 μm BCP treatment [Fig. 13(a)]. Surface analytic techniques showed that the outermost layer of nitrogen doped niobium contains niobium hydrides [21], while recent magneto optical studies have shown that niobium hydrides can act as pinning centers [22]. Effective pinning centers need to have a size on the order of the coherence length, which is in case of niobium 39 nm. It is therefore not surprising that 120 °C baking and HF rinsing, affecting only a few nm of the surface, have no effect on the bulk pinning strength.

C. Feasibility to measure the intrinsic field of first flux entry

For pulsed applications of SRF technology, the maximum achievable accelerating gradient is the figure of merit. The intrinsic material parameter determining the maximum achievable accelerating gradient is the field of first flux entry, H_{entry}. In terms of SRF performance, flux entry at less than 100 nm of the surface, within the London depth, is critical, because it contributes to dissipation and can trigger vortex avalanches and quenches. It has to be noted that flux entry to the area probed by the muons here is not identical to flux entry in the London layer. In the transverse geometry, flux needs to propagate in the millimeter range before being detected by the muons, while in the parallel geometry it is still about 100 μm, corresponding to the low end of the muon stopping distribution, see Fig. 3. Thus, in general, flux entry as probed here is not necessarily related to the maximum gradient of SRF cavities except for the pin-free case. When no pinning exists, flux entry at the surface immediately leads to flux invasion into the bulk. Only in this case can the measurement of flux entry be related to the intrinsic field of first flux penetration.

For pin-free niobium samples we find $\mu_0 H_{\mathrm{entry}} = 176(4)$ mT for the parallel ellipsoid and 179(3) mT for the parallel coin. These values are identical within the resolution of the measurement and therefore confirm that the geometrical approximation (Sec. III B) of the parallel coin as a long strip is applicable here. Both values are close to $\mu_0 H_{\mathrm{c1}}(0\ \mathrm{K}) = 174$ mT as reported by Finnmore [17]. The μSR method therefore allows for a precise measurement of the lower critical field of pin-free uniform superconductors in parallel geometry using the HPF spectrometer. In order to investigate materials with unknown H_{entry} and pinning strength, the coin shape is ideal. It requires, however, that the sample is tested with both spectrometers. First the sample can be measured in parallel geometry, yielding H_{entry} as the field where f_0 deviates from 1. Measuring the sample subsequently in transverse geometry provides an estimate into whether H_{entry} has been overestimated due to strong pinning.

D. Field of first flux entry for low temperature baked samples

Low temperature baking at 120 °C is used to increase the accelerating gradient in superconducting cavities [23]. It is also known to decrease the electron mean free path and therefore H_{c1} [24]. It has been shown that 1.3 GHz cavities which have received such a treatment can be operated in a metastable field-free Meissner state above H_{c1} [25]. An increased intrinsic H_{entry} can be explained by a reduced surface current due to the larger penetration depth of the outer layer as derived by Kubo from solving the London equations with appropriate boundary conditions [26,27]. An alternative explanation is also provided in [27]: If the low temperature baked sample is considered to be an effective bilayer system, as low energy μSR results suggests [28], then there exists an energy barrier at the interface that pushes the vortex towards the material with the larger penetration depth, which in the case of low temperature baked niobium is the outer layer. Based on the results from Romanenko et al. [28] Checchin et al., [29] have proposed yet another mechanism which can describe the enhanced H_{entry}. Solving the dimensionless Ginsburg-Landau equations with a Ginsburg-Landau parameter that changes with depth they find an enhanced surface barrier which is caused by the outer layer with larger penetration depth preventing flux entry at H_{c1}.

Here we find that samples which have been baked at 120 °C have $H_{\mathrm{entry}} > H_{\mathrm{c1}}$ independent of whether the sample has been previously annealed at 1400 °C, see Fig. 13(b). This increase is either caused by pinning in the layer affected by the treatment or an increased intrinsic H_{entry}. Results with coins in transverse geometry have shown that baking at 120 °C does not increase the bulk pinning strength, see Fig. 12(a), suggesting that H_{entry} is indeed enhanced beyond H_{c1}.[2] However, one can argue that the parallel geometry is more sensitive to surface pinning, because the flux lines can pin at the surface and delay migration to the muon implantation site, 130 μm in the bulk. The results suggest that indeed the intrinsic H_{entry} is enhanced by low temperature baking but surface pinning cannot be ruled out completely. This would require the direct measurement of flux penetration in the London layer of a few nm, which is feasible with low energy muon spin

[2]Note that the edge boundary delaying flux entry make measurements in transverse coin not sensitive enough to measure small changes in the intrinsic H_{entry}.

TABLE II. Material parameters of Nb and Nb_3Sn.

Property	Nb	Nb_3Sn
T_c	9.25	18
$\mu_0 H_{c1}(0\ K)$ [mT]	174	38
$\mu_0 H_c(0\ K)$ [mT]	199	520
$\mu_0 H_{sh}(0\ K)$ [mT]	240	380
$\kappa(0\ K)$	1.4	34

rotation [30] or β-NMR [31]. None of these facilities enable measurements in high parallel magnetic fields with the current spectrometers. A dedicated β-NMR spectrometer named beta-SRF is currently under development at TRIUMF. The spectrometer will enable measurements of the flux penetration into the London layer with applied fields up to 200 mT. The new beam-line will compliment the measurements reported here and give new insight to the shielding properties of layered materials.

E. Coated samples

Samples with 2 μm Nb_3Sn coatings on Nb substrates have been investigated. When the maximum field at the surface of the superconductor exceeds H_{c1} of the material (or in case of a surface barrier, the superheating field H_{sh}) the material will enter the mixed phase. Since the film is thin compared to the implantation depth of the muons, Meissner screening could come either from the Nb_3Sn coating or the Nb bulk, depending on temperature and applied field. Literature values of $H_{c1}(0\ K)$ and $H_c(0\ K)$ for niobium of high purity [17] and Nb_3Sn close to stoichiometry [32] are shown in Table II. The superheating field H_{sh} is calculated from [33]:

$$\frac{H_{sh}(\kappa)}{\sqrt{2}H_c} \approx \frac{\sqrt{10}}{6} + \frac{0.3852}{\kappa}, \tag{12}$$

where κ is the Ginsburg-Landau parameter and H_c the critical thermodynamic field.[3] At 2.5 K both the Nb and Nb_3Sn are superconducting and surface currents will be set up in the Nb_3Sn layer until $H_{entry}(T)[Nb_3Sn]$ and in the Nb London layer from $H_{entry}(T)[Nb_3Sn] < H_{interface} < H_{entry}(T)[Nb]$ with the Nb_3Sn coating in the vortex state, where $H_{interface}$ is the field at the interface between the Nb_3Sn layer and the Nb.

The transverse coin results [Fig. 14(a)] indicate that the bulk pinning in the sample is rather weak, when compared to untreated and annealed niobium shown in Fig. 11. This is understandable since the Nb_3Sn application involves a heat treatment to 1100 °C [34]. The transverse ellipsoid results compare closely to the parallel results, which is also indicative of low bulk pinning. In the transverse coin

[3]Note that this equation has been derived using Ginsburg-Landau theory and is therefore strictly only valid close to T_c.

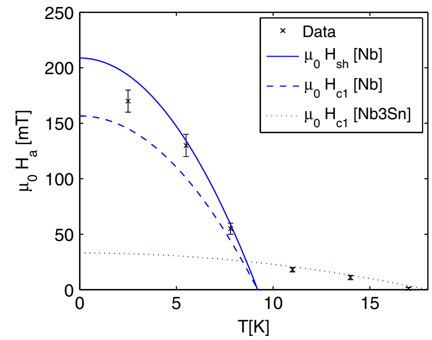

FIG. 15. Measured field of first flux entry of a Nb_3Sn coated Nb ellipsoid. The lines are predictions for the superheating field H_{sh} of Nb and the lower critical field H_{c1} of Nb_3Sn and Nb taking into account the demagnetization factor of this geometry $N = 0.13$.

geometry, f_0 is reduced by about 10% when a field is applied compared to its zero-field value. The reduction in field-free area can be explained by noting that a 1 mm hole is drilled in the coin center to allow coating in the furnace (Fig. 8). Muons passing through this hole are stopped in the sample plate and will sense the magnetic field, spin rotate, and thus reduce f_0.

From the combined results we find that the coating has pushed out the field of first flux entry to about 1.3 times the standard Nb values, meaning that $H_{entry}(0\ K)$ is enhanced to ≈240 mT, which is consistent with the superheating field H_{sh} of niobium. It should be noted, that this does not mean the maximum surface magnetic field of SRF cavities of 2 μm Nb_3Sn on Nb is pushed up to H_{sh} of niobium. Since 2 μm is large compared to the London penetration depth, such a structure will act as a bulk superconductor in an SRF cavity.

Above 9.25 K, the data is consistent with flux entry at the lower critical field H_{c1} of Nb_3Sn [32], see Figs. 14(b) and 15. In [34] H_{c1} was derived by extracting material parameters from Nb_3Sn SRF cavities prepared in the same furnace with the same coating parameters. These results are consistent with our measurements. This indicates that indeed $H_{c1}[Nb_3Sn]$ is measured here and the coating does not delay the penetration of the flux to the muon implantation site 130 μm in the bulk. Furthermore, if this layer would provide pinning and delaying flux entry, for measurements below $T_c[Nb] = 9.25$ K, one would not expect to find a temperature dependence consistent with pure niobium, but rather a relation depending on T_c of Nb_3Sn as well. Furthermore, experiments presented elsewhere on annealed RRR niobium samples coated with MgB_2 layers between 50 and 300 nm also find $H_{entry}(T)$ consistent with $H_{sh}(T)[Nb]$ [35].

VI. CONCLUSION

A technique has been developed to measure the pinning strength and the field of first flux entry, H_{entry}, of SRF materials. If annealed substrates are used it is possible to measure H_{entry} of layered structures and test theoretical predictions for multilayer structures proposed for next generation SRF cavities [26,36,37]. This has encouraged further investigations with different materials and layer thicknesses. The results from these studies are presented elsewhere [35].

ACKNOWLEDGMENTS

This project has been supported by a Marie Curie International Outgoing Fellowship within the EU Seventh Framework Programme for Research and Technological Development. Thanks to PAVAC for providing the formed cutouts, Anna Grassellino for providing the N-doping, Sam Posen, Matthias Liepe, and Daniel Leslie Hall for providing the Nb_3Sn treatments. Thanks to Gerald Morris, Bassam Hitti, Donald Arseneau, Deepak Vyas, Rahim Abasalti, and Iain McKenzie from the TRIUMF CMMS support team. Thanks to Bhalwinder Waraich for fabrication of the ellipsoid and flat coin samples. Thanks to the following people for participating to the experiment: D. Bazyl, D. Azzoni Gravel, Z. He, Y. Ma, L. Yang, Z. Yao, and H. Zhang.

[1] H. Padamsee, T. Hays, and J. Knobloch, *RF Superconductivity for Accelerators*, 2nd ed. (Wiley, New York, 2008).
[2] H. Padamsee, *RF superconductivity: Science, Technology, and Applications* (Wiley, New York, 2009).
[3] A. Grassellino, A. Romanenko, D. Sergatskov, O. Melnychuk, Y. Trenikhina, A. Crawford, A. Rowe, M. Wong, T. Khabiboulline, and F. Barkov, Nitrogen and argon doping of niobium for superconducting radio frequency cavities: A pathway to highly efficient accelerating structures, Supercond. Sci. Technol. **26**, 102001 (2013).
[4] J.-M. Vogt, O. Kugeler, and J. Knobloch, Impact of cool-down conditions at Tc on the superconducting rf cavity quality factor, Phys. Rev. ST Accel. Beams **16**, 102002 (2013).
[5] A. Romanenko, A. Grassellino, O. Melnychuk, and D. A. Sergatskov, Dependence of the residual surface resistance of superconducting radio frequency cavities on the cooling dynamics around Tc, J. Appl. Phys. **115**, 184903 (2014).
[6] S. Posen, M. Checchin, A. C. Crawford, A. Grassellino, M. Martinello, O. S. Melnychuk, A. Romanenko, D. A. Sergatskov, and Y. Trenikhina, Efficient expulsion of magnetic flux in superconducting radiofrequency cavities for high Q_0 applications, J. Appl. Phys. **119**, 213903 (2016).
[7] A. Grassellino, C. Beard, P. Kolb, R. Laxdal, N. S. Lockyer, D. Longuevergne, and J. E. Sonier, Muon spin rotation studies of niobium for superconducting rf applications, Phys. Rev. ST Accel. Beams **16**, 062002 (2013).
[8] A. Yaouanc and P. D. De Reotier, *Muon spin rotation, relaxation, and resonance: Applications to condensed matter* (Oxford University Press, New York, 2011), Vol. 147.
[9] A. Schenck, *Muon Spin Rotation Spectroscopy: Principles and Applications in Solid State Physics* (Adam Hilger, London, 1985).
[10] S. Gheidi, T. Buck, T. Dehn, T. Junginger, R. R. Kiefl, R. Laxdal, and G. Morris, Muon Spin Rotation on Treated Nb Samples in Parallel Field Geometry, in *17th International Conference on RF Superconductivity, Whistler, BC, Canada* (JACOW, Geneva, Switzerland, 2015), p. 210.
[11] J. F Ziegler, D. Matthias M. D. Ziegler, and J. P. Biersack, SRIM–The stopping and range of ions in matter, Nucl. Instrum. Methods Phys. Res., Sect. B **268**, 1818 (2010).
[12] R. S. Hayano, Y. J. Uemura, J. Imazato, N. Nishida, T. Yamazaki, and R. Kubo, Zero- and low-field spin relaxation studied by positive muons, Phys. Rev. B **20**, 850 (1979).
[13] J. E. Sonier, Muon spin rotation studies of electronic excitations and magnetism in the vortex cores of superconductors, Rep. Prog. Phys. **70**, 1717 (2007).
[14] D.-X. Chen, E. Pardo, and A. Sanchez, Fluxmetric and magnetometric demagnetizing factors for cylinders, J. Magn. Magn. Mater. **306**, 135 (2006).
[15] E. H. Brandt, Superconductors in realistic geometries: Geometric edge barrier versus pinning, Physica (Amsterdam) **332C**, 99 (2000).
[16] D.-X. Chen, E. Pardo, and A. Sanchez, Radial magnetometric demagnetizing factor of thin disks, IEEE Trans. Magn. **37**, 3877 (2001).
[17] D. K. Finnemore, T. F. Stromberg, and C. A. Swenson, Superconducting properties of high-purity niobium, Phys. Rev. **149**, 231 (1966).
[18] S. Posen, M Liepe, and D. L. Hall, Proof-of-principle demonstration of Nb3Sn superconducting radiofrequency cavities for high Q_0 applications, Appl. Phys. Lett. **106**, 082601 (2015).
[19] S. Casalbuoni, E. A. Knabbe, J. Kötzler, L. Lilje, L. Von Sawilski, P. Schmüser, and B. Steffen, Surface superconductivity in niobium for superconducting RF cavities, Nucl. Instrum. Methods Phys. Res., Sect. A **538**, 45 (2005).
[20] D. Ashavai, P. Dhakal, A. A Polyanskii, and G. Ciovati, Flux pinning characteristics in cylindrical niobium used for superconducting radio frequency cavity fabrication, Supercond. Sci. Technol. **25**, 065014 (2012).
[21] Y. Trenikhina, A. Grassellino, O. Melnychuk, and A. Romanenko, in *17th International Conference on RF Superconductivity (SRF2015), Whistler, BC, Canada, 2015* (JACOW, Geneva, Switzerland, 2015), p. 223.
[22] J. Köszegi, O. Kugeler, D. Abou-Ras, J. Knobloch, and R. Schäfer, A magneto-optical study on magnetic flux expulsion and pinning in high-purity niobium, J. Appl. Phys. **122**, 173901 (2017).
[23] B. Visentin, Q-Slope at high gradients: Review of experiments and theories, in *Proceedings of the 11th International Workshop on RF Superconductivity, Lübeck, Germany, 2003* (JACOW, Geneva, Switzerland, 2003), p. 199.
[24] G. Ciovati, Effect of low-temperature baking on the radio-frequency properties of niobium superconducting cavities for particle accelerators, J. Appl. Phys. **96**, 1591 (2004).
[25] S. Posen, N Valles, and M. Liepe, Radio Frequency Magnetic Field Limits of Nb and Nb_3Sn, Phys. Rev. Lett. **115**, 047001 (2015).

[26] T. Kubo, Y. Iwashita, and T. Saeki, Radio-frequency electromagnetic field and vortex penetration in multilayered superconductors, Appl. Phys. Lett. **104**, 032603 (2014).

[27] T. Kubo, Multilayer coating for higher accelerating fields in superconducting radio-frequency cavities: A review of theoretical aspects, Supercond. Sci. Technol. **30**, 023001 (2017).

[28] A. Romanenko, A. Grassellino, F. Barkov, A. Suter, Z. Salman, and T. Prokscha, Strong Meissner screening change in superconducting radio frequency cavities due to mild baking, Appl. Phys. Lett. **104**, 072601 (2014).

[29] M. Checchin, A. Grassellino, M. Martinello, S. Posen, A. Romanenko, and J. Zasadzinski, Ultimate Gradient Limitation in Niobium Superconducting Accelerating Cavities, in *7th International Particle Accelerator Conference, Busan, Korea* (JACOW, Geneva, Switzerland, 2016), p. 2254.

[30] T. Prokscha, E. Morenzoni, K. Deiters, F. Foroughi, D. George, R. Kobler, A. Suter, and V. Vrankovic, The new μE4 beam at PSI: A hybrid-type large acceptance channel for the generation of a high intensity surface-muon beam, Nucl. Instrum. Methods Phys. Res., Sect. A **595**, 317 (2008).

[31] G. D. Morris, *ISAC and ARIEL: The TRIUMF Radioactive Beam Facilities and the Scientific Program* (Springer, New York, 2013), p. 173.

[32] A Godeke, *Nb_3sn for Radio Frequency Cavities* (Lawrence Berkeley National Laboratory, Berkeley, CA, 2006).

[33] M. K. Transtrum, G. Catelani, and J. P. Sethna, Superheating field of superconductors within Ginzburg-Landau theory, Phys. Rev. B **83**, 094505 (2011).

[34] S. Posen and M. Liepe, Advances in development of Nb_3Sn superconducting radio-frequency cavities, Phys. Rev. ST Accel. Beams **17**, 112001 (2014).

[35] T. Junginger, W. Wasserman, and R. E. Laxdal, Superheating in coated niobium, Supercond. Sci. Technol. **30**, 125012 (2017).

[36] A. Gurevich, Enhancement of rf breakdown field of superconductors by multilayer coating, Appl. Phys. Lett. **88**, 012511 (2006).

[37] A. Gurevich, Maximum screening fields of superconducting multilayer structures, AIP Adv. **5**, 017112 (2015).